

# Coronal Non-Thermal and Doppler Plasma Flows Driven by Photospheric Flux in 28 Active Regions

James MCKEVTIT,<sup>1,2,\*</sup> Sarah MATTHEWS,<sup>1</sup> Deborah BAKER,<sup>1</sup> Hamish A. S. REID,<sup>1</sup> David H. BROOKS,<sup>3,1</sup> Ignacio UGARTE-URRA,<sup>4</sup> Peter R. YOUNG,<sup>5,6</sup> Teodora MIHAILESCU,<sup>7</sup>

<sup>1</sup>University College London, Mullard Space Science Laboratory, Holmbury St Mary, Dorking, Surrey, RH5 6NT, UK

<sup>2</sup>University of Vienna, Institute of Astrophysics, Türkenschanzstrasse 17, Vienna A-1180, Austria

<sup>3</sup>Computational Physics, Inc., Springfield, VA 22151, USA

<sup>4</sup>Space Science Division, Naval Research Laboratory, Washington, DC 20375, USA

<sup>5</sup>NASA Goddard Space Flight Center, Solar Physics Laboratory, Heliophysics Science Division, Greenbelt, MD 20771, USA

<sup>6</sup>Department of Mathematics, Physics and Electrical Engineering, Northumbria University, Newcastle upon Tyne, UK

<sup>7</sup>INAF Osservatorio Astronomico di Roma, Monte Porzio Catone 00078, Italy

\*E-mail: james.mckevitt.21@ucl.ac.uk

ORCID: 0000-0002-4071-5727, 0000-0001-9346-8179, 0000-0002-0665-2355, 0000-0002-6287-3494, 0000-0002-2189-9313, 0000-0001-5503-0491, 0000-0001-9034-2925, 0000-0001-8055-0472

## Abstract

Magnetohydrodynamic (MHD) waves and/or the braiding of magnetic field lines are largely thought to be responsible for heating the solar corona, both being mechanisms which are driven by the Sun's photospheric magnetic field. Recent modelling work leads us to expect that such heating mechanisms would be seen in the excess broadening (non-thermal velocity) of coronal spectral emission lines and that larger magnitudes of photospheric magnetic flux would generate more heating, but a direct connection between magnetic flux and spectral line broadening has been difficult to establish. We combine measurements of the photospheric magnetic field from SDO/HMI and non-thermal velocity in  $\log T \sim 6.2$  coronal plasma from Hinode/EIS for 28 active regions and find a moderate correlation between the two exists in quiescent active regions, consistent with the photospheric field injecting upward Poynting flux into the solar corona and causing coronal heating. We find that no strong correlation with coronal composition makes it difficult to distinguish between MHD wave heating and magnetic field braiding heating using these diagnostics with current instrumentation.

**Keywords:** Sun: corona — Sun: photosphere — Sun: magnetic fields — Sun: UV radiation

## 1 Introduction

The cause of the solar corona's extreme million-degree temperature remains a fundamental open problem in solar physics. Two broad classes of models are thought to heat coronal plasma: nanoflare or reconnection heating, in which countless small-scale magnetic reconnection events dissipate stored magnetic energy into heat (e.g., Parker 1988), and wave or turbulence heating, in which magnetohydrodynamic (MHD) waves (e.g. Alfvén or kink waves) launched by convective motions propagate upward and dissipate their energy in the corona (e.g., Alfvén 1947; Ionson 1978). In both scenarios, the source of energy is the Sun's magnetic field and convective motions at the photosphere, which inject Poynting flux into the corona. In the nanoflaring scenario, footpoint shuffling can tangle (braid) coronal field lines and generate numerous current sheets, releasing energy in many small reconnection bursts. Similarly in the wave heating scenario, twisting motions or vortex flows at the photosphere can drive MHD waves which, through non-linear wave-wave interactions, cascade to smaller scales in a turbulent spectrum and at small enough scales dissipate as heat. Through these processes, photospheric motions effectively act as an energy pump, injecting upward Poynting flux that can balance the enormous radiative and conductive losses of active region plasma. Estimates by Parker (1983) and subsequent modelling by

e.g. Yeates et al. (2014) suggest that the energy input from braiding could be sufficient to explain the coronal conductive and radiative losses in active regions. Furthermore, several observations by for instance Viall & Klimchuk (2012); Ishikawa et al. (2017) find evidence consistent with the nanoflare heating model (Klimchuk 2015). There have been suggestions that coronal heat originates in the chromosphere (e.g., Aschwanden et al. 2007; De Pontieu et al. 2009), but subsequent work finds differently (e.g., Klimchuk & Bradshaw 2014; Patsourakos et al. 2014). Meanwhile McIntosh et al. (2011) have found evidence for Alfvénic waves sufficient to heat the quiet corona. However, Alfvén speeds sufficient to explain coronal heating throughout the real density-stratified corona have not yet been observed (Van Doorsselaere et al. 2020; Morton et al. 2023).

Both these nanoflare and MHD wave heating mechanisms rely on injection of energy into the corona from the photosphere, quantified by the vertical Poynting flux. It is known that this Poynting flux is proportional to the photospheric magnetic flux, with Welsch (2015) finding on the order of  $10^5$  erg/s of energy are injected into the corona per Mx at the photosphere. This implies that the photospheric magnetic flux of an active region is intimately linked to the energy input available for heating and plasma motions. Indeed, Pevtsov et al. (2003) presented results suggesting such a relationship in all active stars.

Spectroscopic observations of coronal plasma, required to develop our understanding of these mechanisms, have been primarily performed by the extreme ultraviolet (EUV) imaging spectrometer (EIS; Culhane et al. 2007) onboard the Hinode spacecraft (Kosugi et al. 2007) over the last nearly 20 years. Spectral emission lines are typically observed by Hinode/EIS as quasi-Gaussian distributions, which are also sometimes considered as  $\kappa$ -distributions or similar with large wings (see interesting discussion in Lörinčík et al. (2020)). Such functions are fitted to the observed spectral lines, with their widths representing the thermal broadening of the plasma, broadening due to the point spread function of the instrument, and then additional Doppler broadening which has previously been attributed to a variety of processes (Del Zanna & Mason 2018).

These processes include unresolved Alfvénic motions generated by convective footpoint driving (Hassler et al. 1990; Banerjee et al. 2009), turbulence induced by impulsive heating events such as nanoflares (Patsourakos & Klimchuk 2006), and the superposition of small-scale flows that remain unresolved within the instrumental resolution (Hara et al. 2008). Other proposed contributions include line-of-sight integration effects across multiple structures (Feldman 1983), and broadening produced by interchange reconnection and associated rarefaction waves in coronal outflow regions (Bradshaw et al. 2011). The stochastic dynamics of spicules and related jet-like features (causing asymmetric broadening) have also been suggested (De Pontieu et al. 2009), as has non-equilibrium ionisation, particularly in rapidly evolving transition region and coronal plasma (Bradshaw & Mason 2003; Dzifčáková & Kulinová 2011). However, neither spicule- or non-equilibrium ionisation-related heating are currently thought to make a notable contribution to excess broadening in quiescent coronal plasma around 1 MK.

Where this excess broadening is expressed as an equivalent velocity (non-thermal velocity), previous simulation work has found this to be correlated with magnetic braiding-induced turbulence (Pontin et al. 2020) and Alfvén wave turbulence (Asgari-Targhi et al. 2024). In the case of braiding-type heating, plasma is thought to be initially heated to flare-like temperatures on the order of  $\log T \sim 7$  and then cool. A study by Winebarger & Warren (2004) found that in the case that active region loops are impulsively heated, temperature and density measurements at lower temperatures are insufficient to recover information about what may have caused their previous heating. However, the aforementioned modelling by Pontin et al. (2020) produced braiding-induced broadening at the cooler coronal  $\log T \sim 6.2$ , raising the question of whether broadening might be a parameter that retains some information about previous heating.

As coronal spectral line broadening may be observed where coronal heating has occurred, that coronal heating is a product of Poynting flux, and that Poynting flux is increased above stronger photospheric magnetic fields, we might then see a relationship between this photospheric magnetic field strength and excess spectral line broadening in the corona. However, Brooks & Warren (2016) reported no significant trend between the excess broadening in high temperature active region loops and the active region's unsigned photospheric magnetic field strength when considering 15 active regions. They concluded that the limited broadening we observe in the cooling phase of coronal loops is all that remains well after the energy release process is complete. Their study was focused on active region loop measurements, but observations of different features or plasma including different structures across a whole active region might yield a different result. It

would also then be interesting to consider the evolution of an active region's excess broadening with age as when its photospheric magnetic field disperses, it could be expected that the excess broadening would decrease either because the region's magnetic stressing and nanoflaring subside and/or because plasma conditions become more uniform.

As both Alfvén waves and nanoflares should cause excess spectral line broadening, an additional spectral diagnostic is needed to distinguish these mechanisms observationally, and here we turn to composition measurements.

The composition of coronal plasma can be determined using the First Ionization Potential (FIP) effect, which describes the enhancement or depletion of elemental abundances in the solar corona relative to their photospheric values (Laming 2015). Elements with a relatively low-FIP are typically enhanced in abundance in the corona compared to the photosphere, whereas high-FIP elements tend to maintain their photospheric abundance in the corona. This enhancement is quantified using the FIP bias parameter which is the ratio of the coronal elemental abundance to the photospheric elemental abundance. One leading theory explaining the FIP effect describes it as driven by the ponderomotive force associated with MHD waves, like Alfvén waves, propagating through or reflecting from the chromosphere. The ponderomotive force acts selectively on chromospheric ions but not on neutral atoms, leading to elemental fractionation (Laming 2012). This effect is observed using Hinode/EIS by comparing the intensities of low-FIP elements (typically Si) and high-FIP elements (like S), additionally taking into account temperature- and density-related effects (e.g., Brooks et al. 2015). A previous study by Baker et al. (2013) found a moderate correlation between the non-thermal velocity and FIP bias of coronal plasma in the footpoints of an active region, supportive of the ponderomotive force model and potentially indicative of Alfvén waves. On larger scales, however, the relationship is unexplored, and complicated by the fact there are competing views on the location and driver of the MHD waves associated with the elemental fractionation (Laming 2017; Martínez-Sykora et al. 2023).

In this study, we investigate the relationships between coronal non-thermal velocity and various other active region properties in 28 active regions captured by full-Sun Hinode/EIS spectral scans. Comparable studies typically rely on small samples of dedicated active region observations, which introduce a bias toward compact regions or fail to capture entire structures given the limited Hinode/EIS field of view. The full-disk approach (combining observations to cover the full Sun) captures an unbiased variety of active regions, including extended structures with very different morphologies that would not otherwise be studied. We combine this Hinode/EIS data with photospheric magnetic flux measured by the Helioseismic Magnetic Imager (HMI; Scherrer et al. 2012) onboard the Solar Dynamics Observatory (SDO; Pesnell et al. 2012), active region type and age as determined by Mihalea et al. (2022), and coronal composition as calculated by Brooks et al. (2015), to address: 1) if the modelled proportionality between magnetic flux and upward Poynting flux translates to statistically-significant observed heating-induced line broadening on active region scales, 2) if FIP bias and line broadening measurements can help distinguish between heating mechanisms, 3) if any observed heating signatures depend on active region age and evolutionary stage. We make the code to automatically construct Hinode/EIS full disks available<sup>1</sup>.

<sup>1</sup> This paper uses version 0.1.2: <https://doi.org/10.5281/zenodo.17641183>. The source code and ongoing development are available at: [https://github.com/astrobaker/Hinode\\_EIS\\_Full\\_Disks](https://github.com/astrobaker/Hinode_EIS_Full_Disks)

## 2 Observations

### 2.1 EUV Observations

We use three full-disk mosaic data sets taken by the scanning slit EUV spectrometer Hinode/EIS between (times in UT) 09:37 on 16 January 2013 and 06:00 on 18th January 2013 (disk 1), 09:14 on 1 April 2015 and 00:45 on 3 April 2015 (disk 2), and 10:27 on 18 October 2015 and 00:26 on 20 October 2015 (disk 3). During these three windows, Hinode/EIS was operating low-cadence, wide field-of-view active region studies, positioned to cover the whole solar disk in 26 separate rasters.

These rasters are positioned so that together they cover the whole solar disk, where some overlap between the rasters is present. Due to the differential rotation of the solar surface beneath the spacecraft, and the fact the rasters to cover one full disk take just less than two days to complete, the rasters should be adjusted to positions correct relative to one another, and overlap regions handled with care.

We use the flux-conserving spherical polygon intersection method from `Astropy` (The Astropy Collaboration et al. 2022) to position our rasters appropriately relative to the first raster of each full disk. Regions where multiple rasters covered the same region on the Sun will be measured differently by the spectrometer, partly due to instrumental noise effects (see McKevitt et al. (2026)) and partly because in the sometimes many hours between rasters, plasma in that region will have changed. In the coronal intensity (Fe XII 195.119 Å  $\log T \sim 6.2$ ) full disk maps seen in Figure 1 we take the raster contributing the highest intensity to each pixel.

We note that the rasters of the first full disk were ordered differently to the other two we consider here, which is why the white stripes (indicating no data is available for that part of the disk) appear different (EIS studies 491 and 544 were used)<sup>2</sup>. These studies complete a scanning raster, with 123 pointing positions taken sequentially from west to east with a 2 arcsec slit and with a scan step size of 4 arcsec, meaning the active regions were recorded with quasi-4 arcsec spatial resolution.

#### 2.1.1 Bulk flows

To measure coronal plasma motions we used the strong Fe XII 195.119 Å ( $\log T \sim 6.2$ ) coronal line. This line has the highest signal-to-noise ratio of any coronal lines observed by Hinode/EIS (Young et al. 2007), and as the full disk mosaics include coverage of many quiet Sun areas with low signal it provided the lowest  $\chi^2$  residual when fitting the observed spectra.

We perform a two-component Gaussian fitting for each pixel in each raster scan using `MPFit` (Markwardt 2009), as implemented in the `EISPACE` code (Weberg et al. 2023), with a separate component for the Fe XII 195.119 Å and Fe XII 195.179 Å blended lines respectively (Del Zanna & Mason 2005), where a fixed 0.06 Å offset in the components is imposed. Taking the fit parameters of the Fe XII 195.119 Å component, we calculate the line of sight Doppler velocity using

$$v_{\text{Doppler}} = \frac{c(\lambda_{\text{obs}} - \lambda_0)}{\lambda_0}, \quad (1)$$

where  $c$  is the speed of light,  $\lambda_{\text{obs}}$  is the observed wavelength at peak intensity of the fit, and  $\lambda_0$  is the rest wavelength of the line. We found no pixels to be saturated during these observations and so did not exclude any for this reason from fitting. The accuracy

//github.com/jamesmckevitt/eismaps

<sup>2</sup> <https://solarb.mssl.ucl.ac.uk/SolarB/>

of Doppler velocity measured by Hinode/EIS is known to be approximately 5 km/s (Culhane et al. 2007; Young et al. 2012; see also Kamio et al. 2010 for an interesting discussion on instrument uncertainties.)

As we consider active regions at different positions on the disk and there is known to be some dependence on the line-of-sight velocity with disk position (Démoulin et al. 2013), we normalise for this by adjusting each pixel's measured line-of-sight Doppler velocity for its position on the solar disk using the equation

$$v_{\text{norm}} = \frac{v_{\text{Doppler}}}{\cos \theta}, \quad (2)$$

where  $\theta$  is the angle between the line of sight and the normal to the solar surface. This is a simplification which assumes any Doppler velocities measured across the disk are observations made at an angle to plasma flowing normal to the surface. The alternative approach would be to avoid the adjustment, where instead measurements of Doppler velocity are washed out towards the limb, making a direct comparison between active regions at different points on the disk difficult. We, therefore, apply this adjustment in our analysis. A consequence of this approach is the amplification of measurement uncertainties near the limb where, as  $\cos \theta$  becomes small, the effective noise is increased. This broadens the distribution of plasma measured with near-zero velocities. However, as seen in our results later, this affects only active regions at the very edge of the disk and is seen only in lower pixel counts in the narrow range of  $|v_{\text{norm}}| \lesssim 1$  km/s.

#### 2.1.2 Non-thermal motions

We convert the width of the fitted Gaussian to a non-thermal velocity ( $v_{nt}$ ), that being the measured width of the observed spectral lines unexplained by the thermal and instrumental widths expressed as a velocity, using

$$\text{FWHM}_o^2 = \text{FWHM}_i^2 + 4 \ln 2 \left( \frac{\lambda}{c} \right)^2 (v_t^2 + v_{nt}^2), \quad (3)$$

where  $\text{FWHM}_o$  and  $\text{FWHM}_i$  refer to the observed and instrumental full width at half maximum values respectively, and where  $\lambda$  and  $v_t$  refer to the emission line rest wavelength and the associated thermal velocity respectively. We use the instrumental width along the slit determined by Young (2011), and the thermal widths from `eis_width2velocity` in the EIS software tree in Solarsoft.

The uncertainty in the instrumental width can be combined with the statistical error in the fitted Gaussian - partly caused by uncertainty in the measurement of each point in the emission line - using standard error propagation (e.g., Bevington & Robinson 2003) to estimate the error in non-thermal velocity measurements to be approximately 25%. Filtering pixels by their  $\chi^2$  value was attempted to reduce noise but found not to improve the resulting maps. No significant center-to-limb variation is seen in excess spectral line broadening (e.g., Chae et al. 1998), and so no adjustment to these line widths based on position on disk is necessary.

#### 2.1.3 Plasma composition

To probe coronal abundance enhancements we used Si X 258.38 Å (FIP=8.15 eV) and S X 264.23 Å (FIP=10.36 eV) emission. We calculate the FIP bias, where

$$\text{FIP}_{\text{bias}} = \frac{\text{coronal elemental abundance}}{\text{photospheric elemental abundance}}, \quad (4)$$

using the intensities of the relatively low-FIP Si X 258.38 Å and

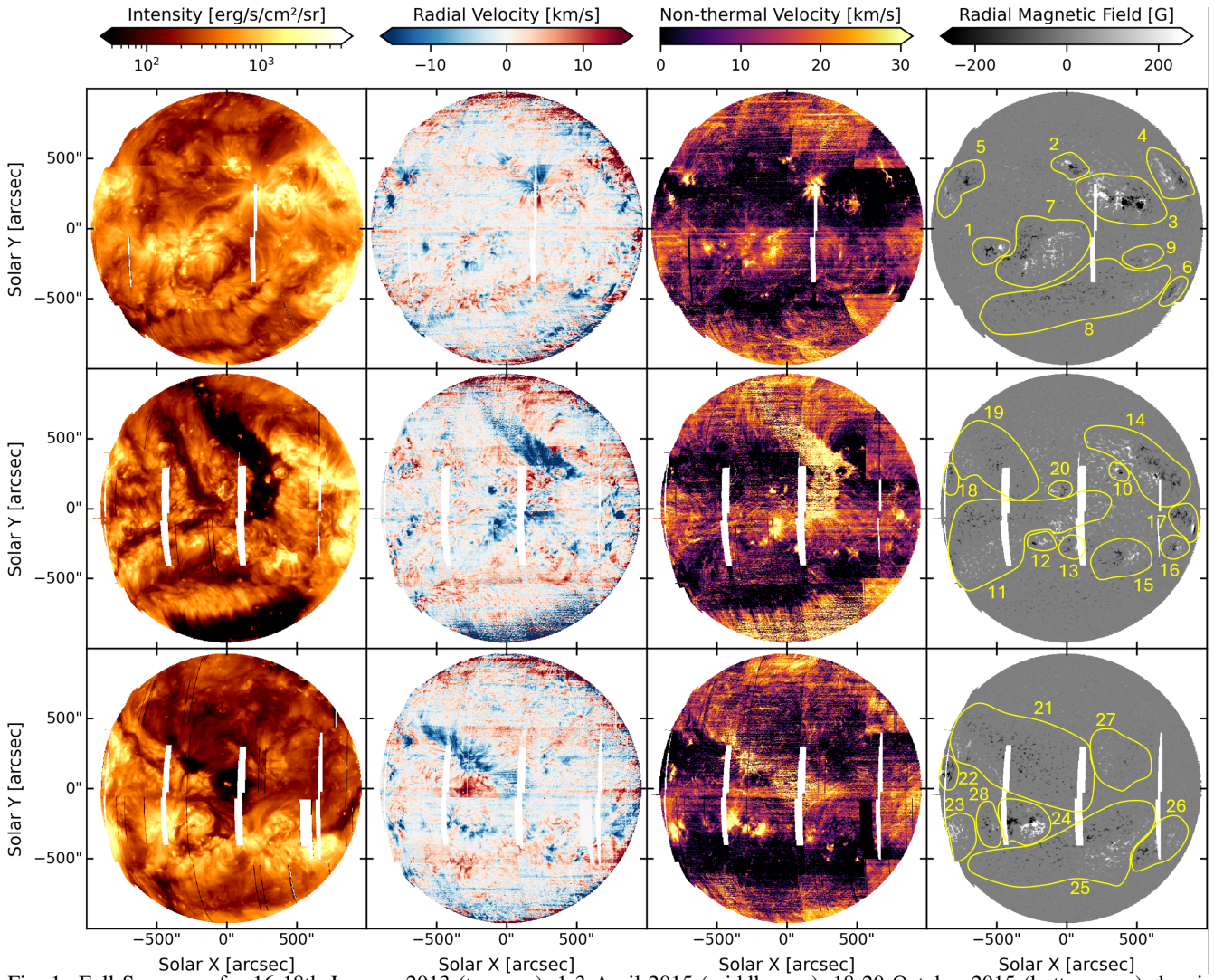


Fig. 1: Full Sun maps for 16-18th January 2013 (top row), 1-3 April 2015 (middle row), 18-20 October 2015 (bottom row) showing from Hinode/EIS the Fe XII 195.119 intensity (far left column), Fe XII 195.119 radial velocity (centre left column), Fe XII 195.119 non-thermal velocity (centre right column), and from SDO/HMI the radial photospheric magnetic field component (far right column). The active regions considered in this study are highlighted with yellow contours and numbered in the right-hand column.

Alt text: Four measurements of full-disk solar maps from three observing periods, each showing intensity, Doppler velocity, non-thermal velocity, and radial magnetic field. Active regions are outlined and numbered.

relatively high-FIP S X 264.23 Å emission lines. This combination is appropriate for studying  $\log T \sim 6.2$ , ideal for the quiescent active regions covered in this study and corresponding with the  $\log T \sim 6.2$  plasma motions we investigate. The FIP values are those presented by Mihăilescu et al. (2022), where the method used is that described in Brooks & Warren (2011) and Brooks et al. (2015) being designed to remove density effects with the Fe XIII 202.04 Å to 203.82 Å ratio (Watanabe et al. 2009; Young et al. 2007), and temperature effects using the Fe lines VIII to XVI to derive the differential emission measure (DEM). These intensities were calibrated using the in-flight radiometric calibration curves provided by Warren et al. (2014). We note a new calibration is available (Del Zanna et al. 2025), but since the calibrations only differ after the observation dates considered here, and to maintain consistency with Mihăilescu et al. (2022), we do not apply the new calibration.

The pointing information of the Hinode/EIS data was corrected by co-aligning the Fe XII 195.12 Å intensity maps with imaging

performed at 193 Å by the Atmospheric Imaging Assembly (AIA; Lemen et al. 2012) onboard SDO. This required only small corrections to both longitude and latitude.

## 2.2 Magnetic Field Observations

We also used data gathered by SDO/HMI at each of the raster times of Hinode/EIS. SDO/HMI generates full-disk vector photospheric magnetograms with a cadence of 12 minutes and at a resolution of about 1 arcsec, with a per-pixel noise level ( $\sigma_{noise}$ ) of about 100 Gauss (Hoeksema et al. 2014). However, we calculate properties of active regions using many pixels ( $N$ ). Since the standard error of sample quantiles (including the median and percentiles we use here) scales as  $\sigma_{noise}/\sqrt{N}$  (Bevington & Robinson 2003), this spatial averaging reduces the statistical uncertainty to the order of 1 G for each active region. Here we consider the radial component  $B_r$  of these 12 minute vector magnetograms as opposed to the higher-cadence line-of-sight magnetograms so as to

AR	Age (days)	Ev. Stage	AR	Age (days)	Ev. Stage
1	5	Spot	15	24	Decayed
2	11	Decayed	16	11	Decayed
3	11	Spot	17	12	Spot
4	13	Spot	18	3	Decayed
5	39	Dispersed	19	58	Filament channel
6	13	Decayed	20	7	Decayed
7	53	Dispersed	21	29	Filament channel
8	189	Filament channel	22	30	Spot
9	13	Decayed	23	27	Spot
10	0.5	Emerging	24	27	Spot
11	120	Filament channel	25	63	Dispersed
12	6	Decayed	26	38	Dispersed
13	8	Decayed	27	35	Dispersed
14	8	Dispersed	28	21	Decayed

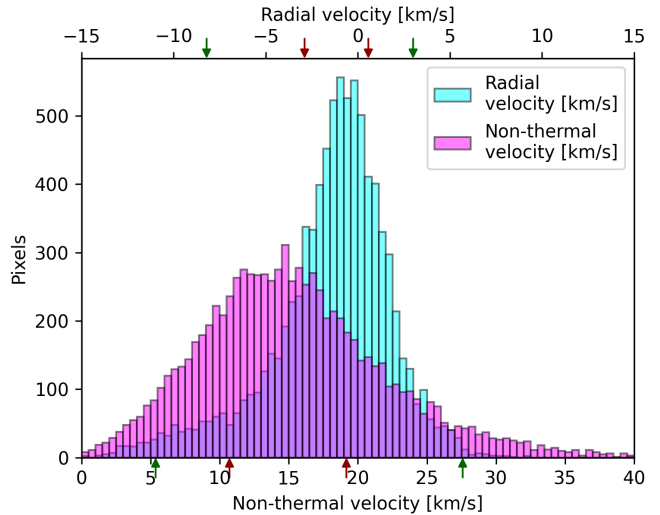
Table 1: Ages and evolutionary stages (Ev. Stage) of active regions (AR) considered in this study, as defined by Mihaleşcu et al. (2022).

use a measure of magnetic field strength normalised to position on the disk, given we are comparing active regions at various disk positions. We acknowledge that photospheric magnetic flux measurements from HMI are increasingly affected by noise towards the limb (Hoeksema et al. 2014). However, as we are looking at active regions with strong polarities and we only find this affect very barely noticeable in one active region, we find the measurements acceptable for our purposes.

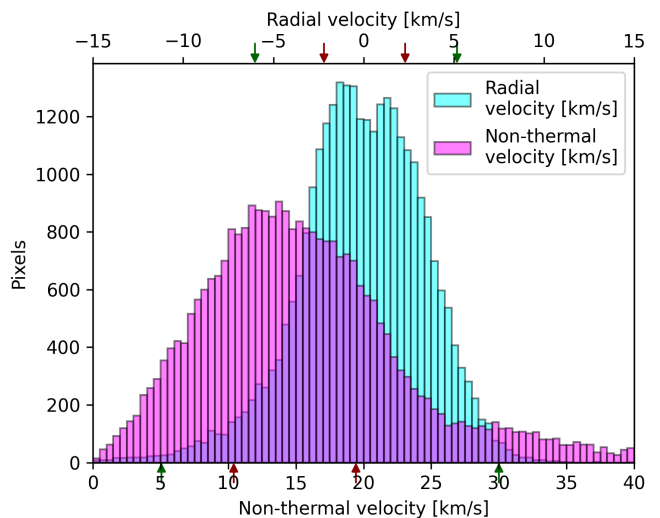
### 2.3 Active Regions

The active regions in this study are those identified and analysed by Mihaleşcu et al. (2022). They were defined by eye using SDO/HMI magnetograms, where boundaries are drawn around concentrations of magnetic flux such that contours are broad enough to include all magnetic flux associated with the active region, but where pixels with a magnetic flux density below 30 G are filtered out of the analysis to avoid considering small-scale background field between the active region field fragments. In a similar fashion, two polarities within each active region are identified. In the region for a given polarity, no opposite polarity field is considered in any analysis. We use the evolutionary stages and ages as identified and defined by Mihaleşcu et al. (2022), summarised in Table 1. Following the ‘emerging’ phase, they define the ‘spot’ phase where bipoles are still clear (peak or early decay), ‘decayed’ (sunspots have disappeared), ‘dispersed’ (active region photospheric field barely distinguishable from quiet Sun), and active regions with filament channels (Mihaleşcu et al. 2022).

We note that the emerging active region (10) appears as an outlier in our results, displaying high non-thermal velocity values. It can be seen in Figure 1 to reside in a coronal hole where stray light in Hinode/EIS is known to artificially increase measured intensity (Young & Viall 2022), affecting non-thermal velocity measurements. Furthermore, it is the smallest active region in our study by area, and so our active region-scale parameters are averaged over less pixels. We, therefore, exclude it from any statistical trends we draw from the data analysis.



(a) Distribution of non-thermal velocity and radial velocity (derived from Doppler velocity) in active region 1.



(b) Distribution of non-thermal velocity and radial velocity (derived from Doppler velocity) in active region 23.

Fig. 2: Histograms of non-thermal velocity and radial velocity (derived from Doppler velocity) measurements in active regions 1 and 23. The 25th and 75th percentiles are shown with red arrows and the 5th and 95th percentiles with green arrows, on the top and bottom axes for their respective measurements.

Alt text: Histograms for two active regions showing distributions of non-thermal velocity and radial velocity. Percentile markers indicate differences in spread.

## 3 Results

### 3.1 Metrics

To quantitatively explore the relationships between coronal velocity and photospheric magnetic field we employ a range of metrics, such as the Pearson product-moment correlation coefficient (hereinafter referred to as  $r$ ) by Bravais (1846). We also use the interquartile range (IQR) - that being the difference between the 75th and 25th percentiles - and the 90% interpercentile range (90% IPR) - that being the difference between the 95th and 5th percentiles - to

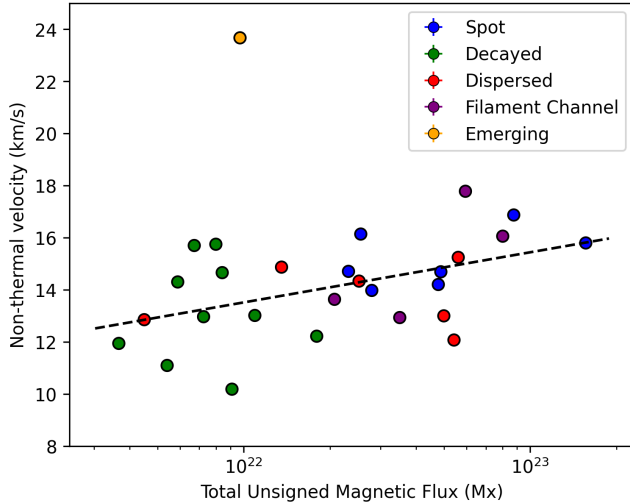


Fig. 3: Total radial unsigned magnetic flux ( $\sum |B_r| \cdot A$ ) against the median non-thermal velocity for each active region, where  $A$  is the pixel area in  $\text{cm}^2$ .

Alt text: Scatter plot comparing non-thermal velocity with total magnetic flux.

quantify the spread of the bulk of the data, and to quantify a range excluding outlying pixels respectively.

Such population distributions of pixels within active regions can be seen in Figure 2. In both the top and bottom panels, for active regions 1 and 23 respectively, we see the velocity distributions have an asymmetric tail towards upflowing velocities. In the top panel (a) we see this somewhat represented in the IQR but much more so in the 90% IPR. In the bottom panel (b), where the active region is larger and encompasses more pixels, we see the tail is not able to make any noticeable impact on the IQR, but is noticeable in the 90% IPR.

In the case of the non-thermal velocity values, both active regions share a similar distribution peaking at between 10 and 15 km/s before tailing off. Active region 23 (panel b) shows some small secondary component peaking at 30 km/s, extending the tail of the distribution for this active region slightly. We see that the IQR is unaffected by this as it is very similar for both active regions, but the 90% IPR reflects this in its upper bound.

We present these distributions and percentiles of two representative active regions to inform the results we show below for the complete dataset, as we use both the IQR and the 90% IPR.

### 3.2 Non-thermal velocity versus Magnetic Field

Figure 3 shows the relationship between non-thermal velocity and the total radial photospheric magnetic flux in Mx in the active regions considered in this study. We see that the decayed active regions, with lower values of total unsigned magnetic flux tend to have slightly lower median non-thermal velocities, whereas the spot type active regions, with the higher total unsigned magnetic flux, appear to have higher median non-thermal velocity values. When including the filament and dispersed-type active regions as well, but excluding the outlier emerging-type active region, we find a moderate positive correlation of  $r=0.48$  when using log-transformed total unsigned magnetic flux. We found a similar correlation between log total unsigned magnetic flux and the 90th percentile non-thermal velocity values.

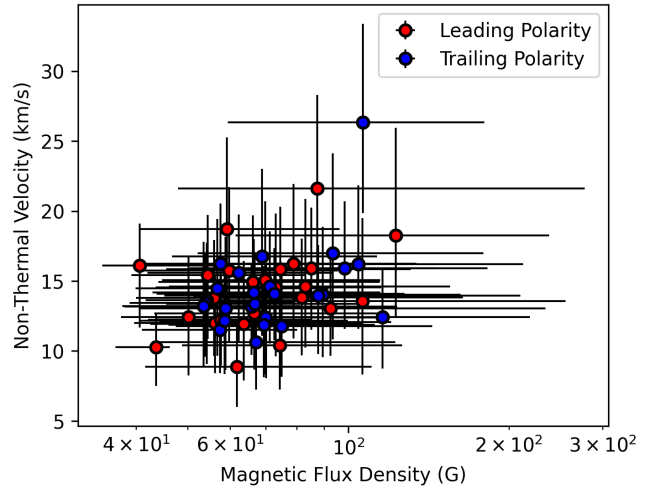


Fig. 4: The relationship between the non-thermal velocity and unsigned magnetic flux density of the leading and trailing polarities of the active regions, with the 25th and 75th percentiles shown with bars and median values with spots.

Alt text: Scatter plot of non-thermal velocity versus unsigned magnetic-flux density for leading and trailing polarities. Median points and percentile ranges are shown, illustrating similar behaviour in both polarities and increasing non-thermal velocity with stronger fields.

We also consider such relationships for the leading and trailing polarities of the active regions in this study, shown in Figure 4. No clear distinction between the behaviour of the polarities is seen here, with both the leading and trailing polarities showing the general trend of above, that higher median non-thermal velocity values are moderately associated with higher median unsigned magnetic flux densities in the active regions.

### 3.3 Non-thermal velocity versus Age

We see no clear correlation between the non-thermal velocity and the age of the active regions, as shown in Figure 5, excluding the emerging active region as an outlier. We similarly observe no clear trend in the spread of non-thermal velocity with age. A consideration of evolutionary stage may be more appropriate for future studies, as we discuss in Section 4.

### 3.4 Non-thermal velocity versus Doppler Velocity

We also consider the relationship between the distribution of the plasma's non-thermal velocity and radial velocity, derived from the line-of-sight Doppler velocity, for each active region.

For several of the spot-type active regions, shown in Figure 6, we see that most plasma with higher non-thermal broadening is also seen to be upflowing where, as non-thermal velocity increases, the upflow velocities increase. The plasma distributions all broadly increase their spread of radial velocities for higher non-thermal velocity values, up to around  $V_{nt} \sim 20 \text{ km/s}$  and a spread of  $V_r \sim 15 \text{ km/s}$ , where the spread decreases and the average flow direction for a given non-thermal velocity becomes increasingly blue-shifted as non-thermal velocity increases. We note active region 4 in the middle left panel doesn't show this relationship as strongly, and displays some increasing red shift to downflowing plasma at  $V_{nt} \sim 20 \text{ km/s}$ . However, this active region is an outlier

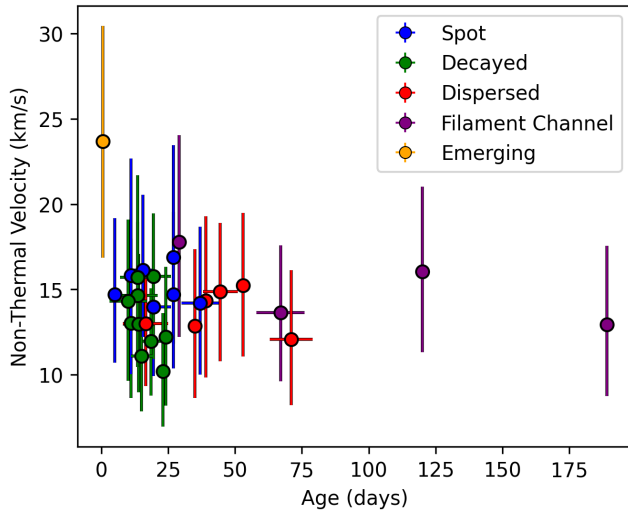


Fig. 5: The relationship between non-thermal velocity and age of the active regions. The median values are shown with circles, and the spread of non-thermal velocities between the 25th and 75th percentiles is shown with bars. For ages, the bars indicate the ranges taken from Mihalea et al. (2022).

Alt text: Scatter plot of non-thermal velocity versus active-region age, with median markers and percentile ranges. Data show wide variability at all ages and no clear age-dependent trend.

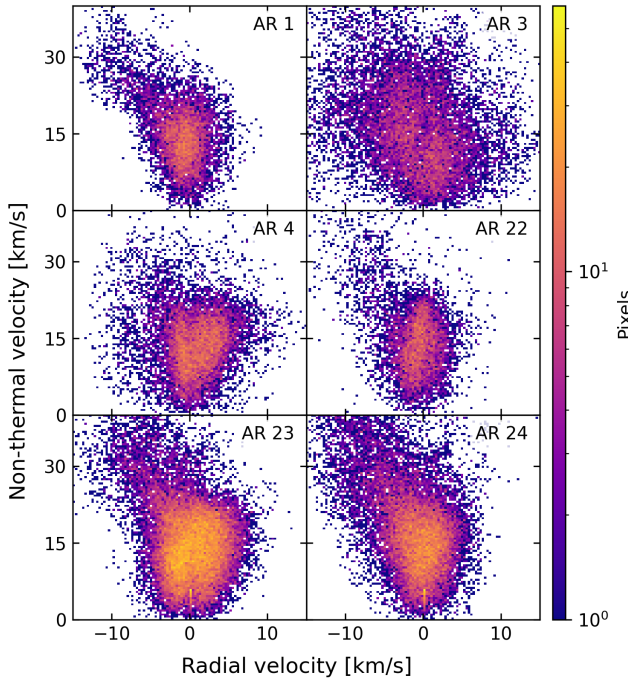


Fig. 6: Histograms of non-thermal velocity against radial velocity (derived from Doppler velocity) for several spot active regions.

Alt text: Six two-dimensional histograms for spot-type active regions showing non-thermal velocity versus radial velocity. Higher non-thermal velocities correspond to increasingly blue-shifted plasma and broader velocity spreads.

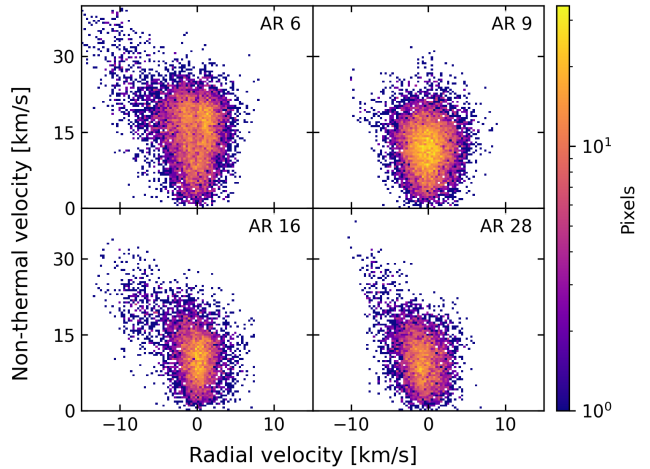


Fig. 7: Histograms of non-thermal velocity against radial velocity (derived from Doppler velocity) for several decayed active regions. Alt text: Four two-dimensional histograms for decayed active regions showing non-thermal velocity versus radial velocity. Moderate upflow trends appear at lower non-thermal velocities, with overall narrower velocity ranges.

amongst all the spot-type active regions, and its plasma distribution is sampled from fewer pixels than, for example, active regions 23 and 24, where the increasing tendency to upflow with higher non-thermal velocities is more prominent.

We show a similar relationship but for some of the decayed active regions in Figure 7. These active regions are smaller in area than the spot-type active regions of Figure 6 and so represent lower statistical certainty in plasma distribution. However, we still see the general trend of increasing upflow with higher non-thermal velocities. The transition to average upflowing plasma for a given non-thermal velocity seems to occur at slightly lower non-thermal velocities than for spot-type active regions, where active regions 6, 16 and 28 all begin their upflow skew just below 15 km/s. These decayed active regions can also be seen to display a lower maximum spread in radial velocity values than for spot-type active regions, where almost all plasma is contained within at most a spread of  $V_r \sim 10$  km/s for a given non-thermal velocity for each active region. We note active region 9 does not appear to display an average radial velocity bias at higher non-thermal velocity values.

We consider the distribution of plasma in a similar way for both the dispersed and filament channel-type active regions in Figure 8 and Figure 9 respectively. In such cases, we are typically sampling many more pixels of plasma as such active region types are larger, as seen by the adjusted colour bars compared with Figures 6 and 7. We see in Figure 8 and Figure 9 that while prominent in some active regions, these dispersed and filament channel-type active regions display a lower tendency to have upflowing plasma at higher values of non-thermal velocity. From the dispersed active regions, active regions 5, 7 and 26 display a clear trend towards upflowing plasma at higher non-thermal velocity values. This trend is loosely apparent in active region 25 but not apparent in active regions 14 or 27. From the filament channel-type active regions, active regions 11 and 21 show some trend towards upflowing plasma at higher non-thermal velocities, but this is subtle compared to the much wider spread of their radial velocities at all values of non-thermal velocity, and not apparent in active regions 8 or 19.

We extend our consideration of non-thermal velocities and radial velocities of plasma in individual active regions to the active

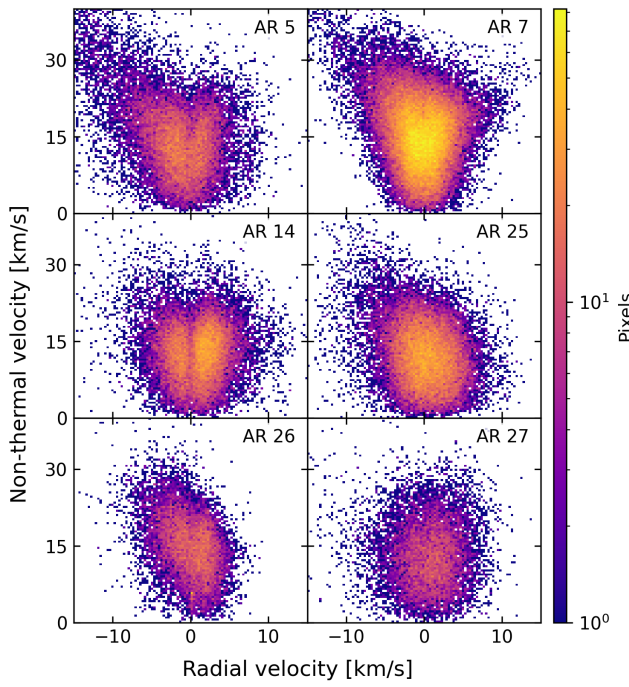


Fig. 8: Histograms of non-thermal velocity against radial velocity (derived from Doppler velocity) for the dispersed active regions.

Alt text: Six two-dimensional histograms for dispersed active regions comparing non-thermal and radial velocities. Some regions show weak upflow trends at higher non-thermal velocities, while others show broad symmetric velocity spreads.

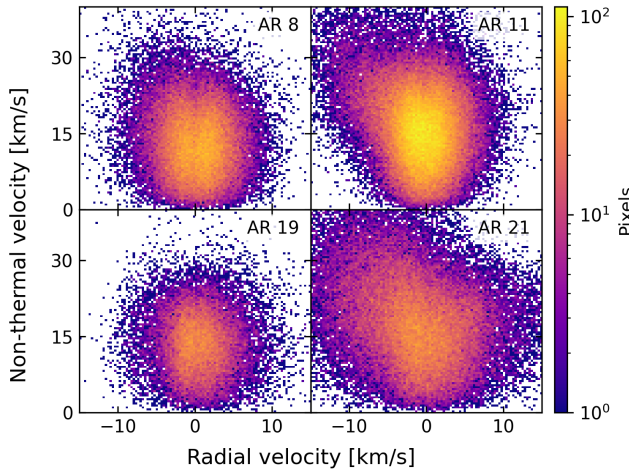


Fig. 9: Histograms of non-thermal velocity against radial velocity (derived from Doppler velocity) for the filament channel active regions.

Alt text: Four two-dimensional histograms for filament-channel active regions showing non-thermal velocity versus radial velocity. Most regions exhibit wide velocity distributions with subtle or absent upflow trends.

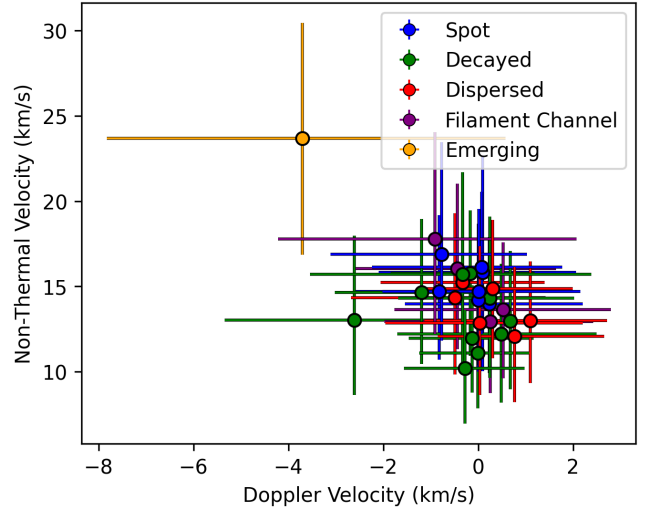


Fig. 10: Scatter plot showing the relationship between non-thermal velocity and radial velocity (derived from Doppler velocity) for all active regions. The median values are shown with circles, and the spread between the 25th and 75th percentiles is also indicated.

Alt text: Scatter plot of median non-thermal velocity versus median radial velocity for all active regions, with percentile bars. Regions with higher non-thermal velocity increasingly show net upflows.

region scale, and consider the median average and IQR spread of velocities for each active region in our study in Figure 10. We see a similar relationship to those in those previous figures (Figures 6, 7, 8 and 9), where higher non-thermal velocities are associated with upflowing plasma. We see that active regions tend to possess a relatively net-zero median average radial velocity up to around  $V_{nt} \sim 15$  km/s, beyond which the median average radial velocities begin a skew towards upflowing plasma. We find a moderate to strong anti-correlation between the median non-thermal velocity and median radial velocity of active regions of  $r=-0.63$ . We additionally considered this relationship for the leading and trailing polarities of the active regions but found no clear distinction between them.

As we saw in Figures 6, 7, 8 and 9, at increasing non-thermal velocity values the spread of radial velocities increases largely symmetrically and then with a bias towards upflowing plasma, i.e., as non-thermal velocity values reach higher values in active regions, the spread of radial velocities increases. We plot such a trend in Figure 11, using the range between the 5th and 95th percentiles of the data to better capture tails in the distribution of upflowing plasma as seen in Figure 2. We see a strong positive relationship between the increase in the spread of non-thermal velocity values and the spread of radial velocities observed in an active region, with  $r=0.78$ .

### 3.5 Non-thermal velocity versus FIP Bias

We examine the relationship between non-thermal velocity and FIP bias in Figure 12. We see no compelling correlation between the two, with moderate median non-thermal velocity values of around 15 km/s corresponding to the entire range of median FIP bias values from 1.4 to 2.1. The relationship between FIP bias and non-thermal velocity in the leading and trailing polarities shows similar results.

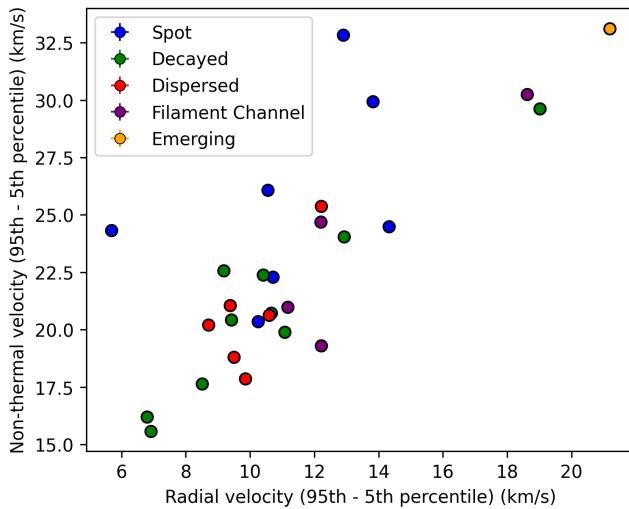


Fig. 11: Difference between the 5th and 95th percentiles of radial velocity (derived from Doppler velocity) against the same range of non-thermal velocity values.

Alt text: Scatter plot showing the relationship between the range (5th–95th percentile) of radial velocities and the corresponding range of non-thermal velocities for each active region. Points show a strong positive correlation between the two spreads.

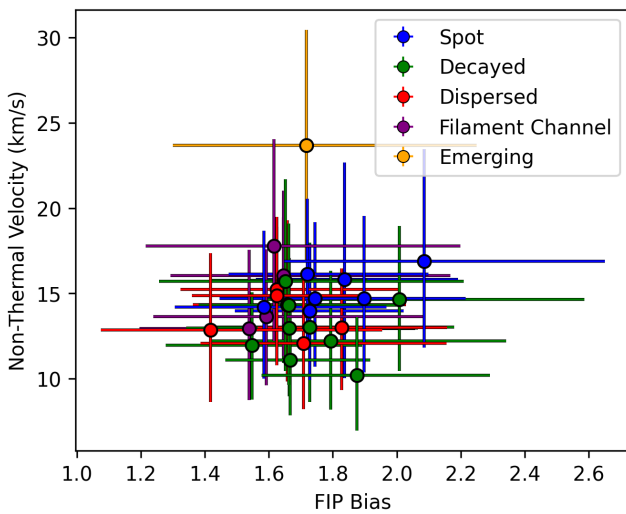


Fig. 12: The relationship between non-thermal velocity and FIP bias for all active regions. The median values are shown with circles, and the spread between the 25th and 75th percentiles is also indicated.

Alt text: Scatter plot of median non-thermal velocity versus median FIP bias for all active regions, with percentile bars. The plot shows no correlation between the two.

## 4 Discussion

### 4.1 Magnetic flux as a driver of non-thermal motions

As we covered in the introduction, observations of non-thermal velocity are thought to be an indicator of MHD waves and/or nanoflares (it is unclear to which degree each mechanism contributes), and previous work has shown simulations of both these mechanisms are capable of reproducing observed non-thermal velocity values in active regions for plasma at coronal temperatures ( $\log T \sim 6.2$ –6.3) (Pontin et al. 2020; Asgari-Targhi et al. 2024). As we have also seen in the literature that these mechanisms are both caused by photospheric magnetic flux, we consider the relationship between magnetic flux and non-thermal velocity across our active regions to validate these relationships.

We find a moderate relationship between the non-thermal velocity of the coronal plasma (at  $\log T \sim 6.2$ ) of an active region and the underlying photospheric magnetic field strength. This indicates that regions with stronger photospheric fields host stronger coronal heating processes, or a higher filling factor of such processes.

Our findings are in agreement with those of Harra & Abramenko (2012) who found a correlation between photospheric magnetic field turbulence (the random motions which are thought to cause magnetic field braiding) and  $\log T \sim 6.2$  non-thermal velocity, indicative of a causal energy release relationship. As work since that of Harra & Abramenko (2012) has shown a quantitative relationship between photospheric magnetic flux and upward-directed Poynting flux (Welsch 2015), it is encouraging therefore that we also find a positive correlation between what is happening in the magnetic field at the photosphere and what we see non-thermally in the coronal plasma.

While Brooks & Warren (2016) did not find a correlation between photospheric magnetic flux and coronal non-thermal velocity, their study considered the relationship between photospheric flux and non-thermal velocity in sections of coronal loops. Harra & Abramenko (2012) considered the correlation between non-thermal velocities from across an entire active region and magnetic flux, as we do, and did find a relationship which they considered indicative of nanoflare heating. Previous studies have shown that non-thermal velocities are typically stronger around active region loop footpoints and the upflows at the active region boundaries. These features contribute to measurements of the whole active region. Indeed Mondal et al. (2025) found that different frequencies of nanoflare appear to heat plasma in different structures of an active region. Therefore, contributions from different heating mechanisms across the active region in locations other than just the loops would be expected to also affect the correlation.

Nanoflare heating is expected to initially occur at  $\log T \gtrsim 7$  (e.g., Ishikawa et al. 2017), and it is not clear whether the signatures of such high temperature heating are still present in the  $\log T \sim 6.2$  plasma we consider here. The correlation we find could indicate such signatures, or could instead be related to MHD wave heating, which should occur closer to  $\log T \sim 6.2$  temperatures (Van Doorslaere et al. 2020; Morton et al. 2023).

When we separate active region leading and trailing polarities in our analysis, we find no clear distinction between them. This is noteworthy as leading polarities are typically more coherent than comparably more dispersed trailing polarities (e.g., Fan et al. 1993). It might be expected that a more fragmented trailing morphology would result in different footpoint shuffling statistics (and thus different braiding heating rates) or different wave heating rates compared to the stable leading spots. However, our re-

sults show that the relationship between non-thermal velocity and magnetic flux remains consistent regardless of polarity. This implies that the mechanism driving the excess broadening depends primarily on the local photospheric magnetic flux density, rather than the global topological coherence of the magnetic flux concentration, at least at the level of difference in coherence between leading and trailing polarities. We discuss this further, comparing spot and decayed active region types, in Section 4.3.

#### 4.2 Connection between non-thermal broadening and bulk flows

The trend of strongly blue-shifted plasma being associated with higher values of non-thermal velocity has been reported many times before, and reviewed extensively by e.g. Doschek (2012). Hara et al. (2008) suggested that this might be due to unresolved upflows at high velocities, a theory largely accepted to explain this relationship (Del Zanna & Mason 2018).

We find that this relationship holds for spot-type, decayed-type, dispersed-type and filament channel-type active regions. This is in agreement with Yardley et al. (2021) who, through a study of 12 active regions, proposed that such high-velocity upflows appear a common feature of all active regions. Their study relied on asymmetric line profiles, and similar analysis of such asymmetries has been performed before (e.g., De Pontieu et al. 2009). While extreme care needs to be taken to avoid introducing systematic errors from the likely asymmetric point spread function of Hinode/EIS (Ugarte-Urra 2010; Warren et al. 2018), such a physical asymmetric profile makes physical sense in the case of strong upflows.

McIntosh et al. (2011) found observational evidence of Alfvénic motions apparently sufficient to heat the quiet corona and accelerate the solar wind, and work of Brooks & Warren (2011) separately established a connection between active region outflows and the solar wind. As it has been shown that Alfvén waves can cause excess spectral line broadening, this ability of Alfvén waves to drive the solar wind through upflowing plasma could be the physical mechanism behind the non-thermal velocity-Doppler velocity relationship we see in Hinode/EIS data in active regions.

As pointed out by Doschek (2012), Hinode/EIS does not quite possess the spatial or spectral resolution to resolve key processes which are responsible for these trends but that SOLAR-C seemed a promising future mission to help address our questions about line broadening. Thirteen years later, SOLAR-C/EUVST is under manufacture and is expected to launch in  $\sim$ 2028 (Shimizu et al. 2020). Forward modelling results show it will be capable of excellent resolution of fundamental flows and structures (McKevitt et al. 2026).

#### 4.3 Non-thermal broadening with age and evolutionary stage

We had considered in our introduction whether because of the dispersal of an active region's magnetic field as it ages (Van Driel-Gesztelyi & Green 2015), and because this would lead to a reduction in Poynting flux available for coronal heating, we would observe a reduction of non-thermal velocity in older active regions. However we found no relationship between non-thermal velocity and active region age. What we did see was that decayed active regions showed lower photospheric magnetic flux and lower non-thermal velocities compared to spot-type active regions (Figure 3). Active regions are known to have different lifetimes (e.g., Ugarte-

Urra et al. 2015), and so comparing their ages may not be as revealing as comparing their evolutionary stages. Indeed, the comparison in Figure 3 between spot- and decayed-type active regions supports this. This suggests a future study considering non-thermal velocity against an active region's progress along its evolutionary cycle may yield a more compelling relationship.

#### 4.4 Elemental fractionation with non-thermal broadening

Baker et al. (2013) found a correlation of  $r=0.36$  between the non-thermal velocity and FIP of plasma in an active region, indicating some connection between the processes causing elemental fractionation and non-thermal broadening. The ponderomotive force model proposes MHD waves are responsible for this elemental fractionation (Laming 2015), where such MHD waves can be seen in non-thermal broadening (e.g., Asgari-Targhi et al. 2024). These MHD waves may be driven by nanoflares in the corona (Laming 2017), or by photospheric motions (Martínez-Sykora et al. 2023).

While our Figure 12 bears some resemblance to the comparable plot for an active region of Baker et al. (2013), we find that on active region scales there appears to be no compelling link between the non-thermal broadening and FIP bias of our active regions. We therefore suggest that the processes governing low-FIP enrichment (e.g. ponderomotive force fractionation) and those setting non-thermal widths at Fe XII formation temperatures are not tightly coupled on active region scales. This appears consistent with studies that distinguish active region cores and upflow regions by composition and dynamics (e.g., Brooks & Warren 2011).

### 5 Summary

The trends we observe across 28 active regions show a potential relationship between active region-scale coronal non-thermal velocity and photospheric magnetic flux, supporting a picture in which larger unsigned photospheric magnetic flux sustains larger Poynting flux into the corona, causing coronal heating through magnetic field braiding nanoflares and/or MHD wave heating. The moderate correlation we find is by no means conclusive, but is higher than could be expected exclusively from nanoflares given we consider active region plasma at  $\log T \sim 6.2$  coronal temperatures. This moderate correlation could therefore indicate active region plasma retains information about high-temperature impulsive heating, or that its heating is due more to lower-temperature MHD wave activity. The full disk observations made by Hinode/EIS enable such statistical studies and should be continued for future missions like SOLAR-C/EUVST, where a higher spatial resolution is expected (McKevitt et al. 2026) and will allow us to better disentangle the mechanisms behind non-thermal emission line broadening.

### Acknowledgments

We thank the reviewer for their comments which greatly improved this manuscript. J.M. was supported by STFC PhD Studentship number ST/X508858/1. Data processing and analysis were performed on Austrian Scientific Computing (ASC) infrastructure (<https://asc.ac.at/>). S.M. and D.B. acknowledge support from UKSA grant No. UKRI920. S.M. was also supported by ESA Contract 1420 No. 4000141160/23/NL/IB, and S.M. and H.A.S.R. are supported by grant 2022-25 ST/W001004/1. S.M.

and D.B. are funded under the Hinode Ops Continuation 2022-25 grant number ST/X002063/1, and D.B. and H.A.S.R. are funded under Solar Orbiter EUI Operations grant number ST/X002012/1 and UKRI980. The work of D.H.B. and I.U.U. was funded by the NASA Hinode program. This research used version 6.0.2 (Mumford et al. 2024) of the SunPy open source software package (The SunPy Community et al. 2020). Data processing and analysis were performed on Austrian Scientific Computing (ASC) infrastructure.

## References

Alfvén, H. 1947, Monthly Notices of the Royal Astronomical Society, 107, 211, publisher: OUP ADS Bibcode: 1947MNRAS.107..211A

Aschwanden, M. J., Winebarger, A., Tsiklauri, D., & Peter, H. 2007, The Astrophysical Journal, 659, 1673

Asgari-Targhi, M., Brooks, D. H., Hahn, M., et al. 2024, The Astrophysical Journal, 968, 7

Baker, D., Brooks, D. H., Démoulin, P., et al. 2013, The Astrophysical Journal, 778, 69

Banerjee, D., Pérez-Suárez, D., & Doyle, J. G. 2009, Astronomy & Astrophysics, 501, L15

Bevington, P. R. & Robinson, K. D. 2003, Data reduction and error analysis for the physical sciences, 3rd edn. (Boston, Mass.: McGraw-Hill)

Bradshaw, S. J., Aulanier, G., & Del Zanna, G. 2011, The Astrophysical Journal, 743, 66

Bradshaw, S. J. & Mason, H. E. 2003, Astronomy & Astrophysics, 401, 699

Bravais, A. 1846, Analyse Mathématique. Sur les probabilités des erreurs de situation d'un point (Paris: Imprimerie Royale)

Brooks, D. H., Ugarte-Urra, I., & Warren, H. P. 2015, Nature Communications, 6, 5947

Brooks, D. H. & Warren, H. P. 2011, The Astrophysical Journal, 727, L13

Brooks, D. H. & Warren, H. P. 2016, The Astrophysical Journal, 820, 63

Chae, J., Schuhle, U., & Lemaire, P. 1998, The Astrophysical Journal, 505, 957

Culhane, J. L., Harra, L. K., James, A. M., et al. 2007, Solar Physics, 243, 19

De Pontieu, B., McIntosh, S. W., Hansteen, V. H., & Schrijver, C. J. 2009, The Astrophysical Journal, 701, L1

Del Zanna, G. & Mason, H. E. 2005, Astronomy & Astrophysics, 433, 731

Del Zanna, G. & Mason, H. E. 2018, Living Reviews in Solar Physics, 15, 5

Del Zanna, G., Weberg, M. J., & Warren, H. P. 2025, The Astrophysical Journal Supplement Series, 276, 42

Doschek, G. A. 2012, The Astrophysical Journal, 754, 153, aDS Bibcode: 2012ApJ...754..153D

Dzifčáková, E. & Kulinová, A. 2011, Astronomy & Astrophysics, 531, A122

Démoulin, P., Baker, D., Mandrini, C. H., & Van Driel-Gesztelyi, L. 2013, Solar Physics, 283, 341

Fan, Y., Fisher, G. H., & Deluca, E. E. 1993, The Astrophysical Journal, 405, 390, aDS Bibcode: 1993ApJ...405..390F

Feldman, U. 1983, The Astrophysical Journal, 275, 367, aDS Bibcode: 1983ApJ...275..367F

Hara, H., Watanabe, T., Harra, L. K., et al. 2008, The Astrophysical Journal, 678, L67

Harra, L. K. & Abramenko, V. I. 2012, The Astrophysical Journal, 759, 104

Hassler, D. M., Rottman, G. J., Shoub, E. C., & Holzer, T. E. 1990, The Astrophysical Journal, 348, L77, aDS Bibcode: 1990ApJ...348L..77H

Hoeksema, J. T., Liu, Y., Hayashi, K., et al. 2014, Solar Physics, 289, 3483

Ionson, J. A. 1978, The Astrophysical Journal, 226, 650, publisher: IOP ADS Bibcode: 1978ApJ...226..650I

Ishikawa, S.-n., Glesener, L., Krucker, S., et al. 2017, Nature Astronomy, 1, 771

Kamio, S., Hara, H., Watanabe, T., Fredrik, T., & Hansteen, V. H. 2010, Solar Physics, 266, 209

Klimchuk, J. A. 2015, Philosophical Transactions of the Royal Society A: Mathematical, Physical and Engineering Sciences, 373, 20140256

Klimchuk, J. A. & Bradshaw, S. J. 2014, The Astrophysical Journal, 791, 60

Kosugi, T., Matsuzaki, K., Sakao, T., et al. 2007, Solar Physics, 243, 3

Laming, J. M. 2012, The Astrophysical Journal, 744, 115

Laming, J. M. 2015, Living Reviews in Solar Physics, 12, 2

Laming, J. M. 2017, The Astrophysical Journal, 844, 153, aDS Bibcode: 2017ApJ...844..153L

Lemen, J. R., Title, A. M., Akin, D. J., et al. 2012, Solar Physics, 275, 17

Lörinčík, J., Dudík, J., Del Zanna, G., Dzifčáková, E., & Mason, H. E. 2020, The Astrophysical Journal, 893, 34

Markwardt, C. B. 2009, Non-linear Least Squares Fitting in IDL with MPFIT, arXiv:0902.2850 [astro-ph]

Martínez-Sykora, J., De Pontieu, B., Hansteen, V. H., et al. 2023, The Astrophysical Journal, 949, 112, publisher: IOP ADS Bibcode: 2023ApJ...949..112M

McIntosh, S. W., De Pontieu, B., Carlsson, M., et al. 2011, Nature, 475, 477

McKevitt, J., Matthews, S., Brooks, D., et al. 2026, submitted

Mihaleacu, T., Baker, D., Green, L. M., et al. 2022, The Astrophysical Journal, 933, 245

Mondal, B., Klimchuk, J. A., Winebarger, A. R., Athiray, P. S., & Liu, J. 2025, The Astrophysical Journal, 980, 75

Morton, R. J., Sharma, R., Tajfirouze, E., & Miriyala, H. 2023, Reviews of Modern Plasma Physics, 7, 17

Mumford, S. J., Freij, N., Stansby, D., et al. 2024, sunpy: A Core Package for Solar Physics

Parker, E. N. 1983, The Astrophysical Journal, 264, 642

Parker, E. N. 1988, The Astrophysical Journal, 330, 474

Patsourakos, S. & Klimchuk, J. A. 2006, The Astrophysical Journal, 647, 1452

Patsourakos, S., Klimchuk, J. A., & Young, P. R. 2014, The Astrophysical Journal, 781, 58

Pesnell, W. D., Thompson, B. J., & Chamberlin, P. C. 2012, Solar Physics, 275, 3

Pevtsov, A. A., Fisher, G. H., Acton, L. W., et al. 2003, The Astrophysical Journal, 598, 1387, aDS Bibcode: 2003ApJ...598.1387P

Pontin, D. I., Peter, H., & Chitta, L. P. 2020, Astronomy & Astrophysics, 639, A21

Scherrer, P. H., Schou, J., Bush, R. I., et al. 2012, Solar Physics, 275, 207, aDS Bibcode: 2012SoPh..275..207S

Shimizu, T., Imada, S., Kawate, T., et al. 2020, in Space Telescopes and Instrumentation 2020: Ultraviolet to Gamma Ray, ed. J.-W. A. Den Herder, K. Nakazawa, & S. Nikzad (Online Only, United States: SPIE), 19

The Astropy Collaboration, Price-Whelan, A. M., Lim, P. L., et al. 2022, The Astrophysical Journal, 935, 167

The SunPy Community, Barnes, W. T., Bobra, M. G., et al. 2020, The Astrophysical Journal, 890, 68

Ugarte-Urra, I. 2010, EIS Point Spread Function, Technical Report 8 (1.0), Naval Research Laboratory, Washington, DC

Ugarte-Urra, I., Upton, L., Warren, H. P., & Hathaway, D. H. 2015, The Astrophysical Journal, 815, 90, aDS Bibcode: 2015ApJ...815..90U

Van Doersselaere, T., Srivastava, A. K., Antolin, P., et al. 2020, Space Science Reviews, 216, 140

Van Driel-Gesztelyi, L. & Green, L. M. 2015, Living Reviews in Solar Physics, 12, 1

Viall, N. M. & Klimchuk, J. A. 2012, The Astrophysical Journal, 753, 35

Warren, H. P., Brooks, D. H., Ugarte-Urra, I., et al. 2018, The Astrophysical Journal, 854, 122

Warren, H. P., Ugarte-Urra, I., & Landi, E. 2014, The Astrophysical Journal Supplement Series, 213, 11

Watanabe, T., Hara, H., Yamamoto, N., et al. 2009, The Astrophysical Journal, 692, 1294

Weberg, M. J., Warren, H. P., Crump, N., & Barnes, W. 2023, Journal of Open Source Software, 8, 4914

Welsch, B. T. 2015, Publications of the Astronomical Society of Japan, 67, 18

Winebarger, A. R. & Warren, H. P. 2004, The Astrophysical Journal, 610, L129

Yardley, S. L., Brooks, D. H., & Baker, D. 2021, Astronomy & Astrophysics, 650, L10

Yeates, A. R., Bianchi, F., Welsch, B. T., & Bushby, P. J. 2014, Astronomy & Astrophysics, 564, A131

Young, P. 2011, Instrumental line widths for the narrow slits of EIS, Technical Report 7 (1.0), Naval Research Laboratory, Washington, DC

Young, P. R., O'Dwyer, B., & Mason, H. E. 2012, *The Astrophysical Journal*, 744, 14

Young, P. R. & Viall, N. M. 2022, *The Astrophysical Journal*, 938, 27

Young, P. R., Zanna, D. G., Mason, H. E., et al. 2007, *Publications of the Astronomical Society of Japan*, 59, S857